Design and scaling of monocentric multiscale imagers

Eric J. Tremblay,[1,3,*] Daniel L. Marks,[2] David J. Brady,[2] and Joseph E. Ford[1]

[1]Department of Electrical & Computer Engineering, University of California San Diego, 9500 Gilman Dr., La Jolla, California 92093-0407, USA

[2]Fitzpatrick Institute for Photonics, Duke University, 101 Science Drive, Durham, North Carolina 27708, USA

[3]Currently with the Institute of Microengineering, EPFL, Station 17 CH-1015 Lausanne, Switzerland

*Corresponding author: eric.tremblay@epfl.ch

Received 29 November 2011; revised 6 May 2012; accepted 8 May 2012;
posted 8 May 2012 (Doc. ID 159061); published 4 July 2012

Monocentric multi-scale (MMS) lenses are a new approach to high-resolution wide-angle imaging, where a monocentric objective lens is shared by an array of identical rotationally symmetric secondary imagers that each acquire one overlapping segment of a mosaic. This allows gigapixel images to be computationally integrated from conventional image sensors and relatively simple optics. Here we describe the MMS design space, introducing constraints on image continuity and uniformity, and show how paraxial system analysis can provide both volume scaling and a systematic design methodology for MMS imagers. We provide the detailed design of a 120° field of viewimager (currently under construction) resolving 2 gigapixels at 41.5 μrad instantaneous field of view, and demonstrate reasonable agreement with the first-order scaling calculation.

OCIS codes: 220.2740, 110.1758, 080.3620, 040.1240.

1. Introduction

Wide-angle gigapixel images are most commonly acquired by angle scanning a conventional high-resolution camera to sequentially form a composite image of the scene [1]. However, the long acquisition time and time lapse between first and last frames make this approach only practical for stationary objects. For some applications such as wide-area persistent surveillance, it is necessary to acquire as large a field of view (FOV) as possible with resolution to allow for long-range operation without loss of object details, all within the time frame of a single acquisition. These requirements easily lead to pixel counts in the multi-gigapixel range and exceed what is available as a monolithic focal plane.

While it is possible to tile smaller sensor die into a larger contiguous defect-free chip, this approach is difficult and costly [2,3]. One approach to avoid a monolithic focal plane is to allow spaces between the image sensor tiles, and use multiple imagers to fill in the interleaving image data, as in DARPA's ARGUS-IS. Here, four co-boresighted imaging systems are multiplexed together to provide a 1.8 gigapixel image over a 60° FOV [4]. This is a successful approach, but to our knowledge it has not been extended to very large FOV, where optical design challenges become more difficult. This is due to a physically large flat image plane for which a wide-angle lens design is possible but difficult since geometric aberrations scale with lens focal length while diffraction does not [5]. A straightforward alternative for very large FOV, high-resolution imaging is the multicamera array, where images are simultaneously composited from an array of independent cameras [6]. However, as we will show, the physical area of the optics becomes prohibitive for a multi-camera array at sufficiently large image sizes.

In 2009, Brady and Hagen proposed a multiscale lens approach, bridging the gap between a single sensor imager and multicamera array [7]. In a multiscale imager, the lens system is separated into a single primary lens and multiple secondary subimagers. The

1559-128X/12/204691-12$15.00/0

objective acts as a common primary optic with shared aperture, but instead of forming a contiguous image plane, the system is divided into multiple image fields by multiple sets of secondary optics, each with its own focal plane. As in a multicamera array, the final image is computationally assembled by stitching together the overlapping FOVs recorded on conventional image sensors. As in a multicamera array, the image is segmented into smaller focal planes, and the secondary optics need to correct aberrations over a limited field angle. But in a multiscale imager, the largest optical elements are shared by all of the secondary subimagers. In the simplest case, the secondary camera array forms a virtual focal plane with demagnifying relay optics, which simplifies the challenge of large focal plane synthesis from smaller arrays [8]. More unique and significant advantages are obtained if individual subimagers correct for aberrations of their corresponding off-axis perspective of the primary lens and for local defocus and exposure requirements. With conventional planar focal plane primary lenses, local aberration correction requires a varying array of field-dependent "freeform" aspheric optics, which have no rotational symmetry and are difficult to fabricate and align. This challenge is alleviated, however, by noting that lens design for a flat field is a legacy constraint of single element focal surfaces, and the primary lens in a multiscale system no longer requires an overall flat focal plane.

Taking the curved focal plane to an extreme results in a hemispherical focal surface centered at the rear principle point of the objective lens. This turns out to be useful, and leads toward an even more symmetric system geometry. The choice of design symmetry shown in Fig. 1 dramatically simplifies the design

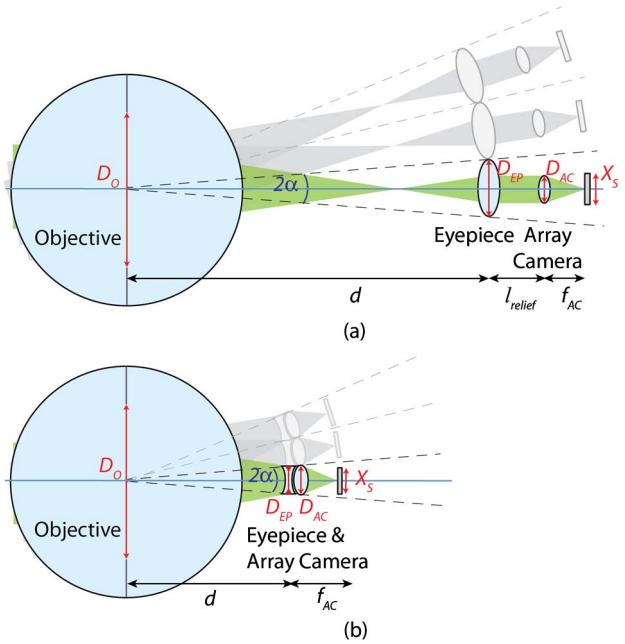

Fig. 1. (Color online) First-order MMS lens models. (a) Keplerian-type and (b) Galilean-type.

and fabrication of wide-field multiscale imagers [9,10]. Making the primary a hemispherically-symmetric monocentric lens [11] means that the aberrations of the primary will be independent of field angle, so that a single on-axis, rotationally symmetric design can be optimum for all the subimagers. Monocentric lenses are a well-established solution to wide angle imaging, with work dating from 1861 with Thomas Sutton's Panoramic Lens, a flint glass sphere filled with water [12] to the present day [13]. Recently, building on their concepts for an omnidirectional spherical imager [14], Cossairt and Nayer implemented a closely related configuration using a glass ball and single element relay lenses. This imager recorded overlapping images on 5 adjacent image sensors, and was demonstrated with angle scanning to acquire and integrate a 1.6 gigapixel image [15].

Multiscale imagers are intrinsically a computational imaging system, and post-detection processing can significantly improve the effective resolution. This does not mean, however, that physical resolution of the detected image is unimportant. While some conventional aberrations, e.g., distortion and field curvature, are easily accounted using computational correction and multiscale design, the impact of defocus, chromatic aberration, spherical aberration, coma, and astigmatism cannot be completely removed in computation. In practice, reducing these aberrations minimizes the computational resources needed, limits visual artifacts in the final image, and allows operation under the broadest lighting conditions.

The optical design of monocentric multiscale (MMS) imagers presents some unique challenges. The subimager fields of view must overlap sufficiently that a complete mosaic image can be computed, with the image resolution maintained into the overlap area. In the overlap regions, light from the primary lens is necessarily divided to illuminate either two or three adjacent image sensors, and the optomechanics used to mount the secondary optical elements tend to introduce dead space between adjacent secondary optics apertures. Control of vignetting losses and stray light suppression are therefore important to maintain an acceptable signal to noise ratio at the subimager field edges. To make the impulse response of all subimager fields identical, the aperture stop for the overall system should lie within the subimager, and the correct choice of subimager geometry and aperture can find a balance between image uniformity and overall light collection efficiency.

In this paper, we define two major classes of MMS imagers, those with and without an internal image plane, and show how imposing constraints on image continuity and uniformity can narrow the design space to valid solutions of both types. We show how a paraxial system analysis can start from basic design parameters (IFOV, FOV, sensor size and pixel pitch) to define the overall lens structure, allowing

volume scaling calculations as well as a systematic design methodology for MMS imagers. With first-order design and scaling relations established we then compare scaling of the MMS lens architecture to that of an equivalent multicamera array. Finally, we illustrate this process with the detailed optical design of a 2 gigapixel 120° FOV imager, which is currently under construction with a large team effort lead by Duke University as part of the DARPA Advanced Wide FOV Architectures for Image Reconstruction (AWARE) program [16].

2. First-Order Models

A MMS lens system can be considered as an array of subimaging systems that relay with local aberration correction the spherical image plane produced by a monocentric objective to an array of conventional flat focal planes. A useful conceptual alternative to this view, which allows for a particularly clean first-order analysis, is to consider the system as a telescope array where the array elements share a common concentric objective lens. Figure 1 shows the simplified lens arrangement for one channel of the MMS system with Keplerian and Galilean type arrangements. A Keplerian telescope uses a positive primary lens and positive secondary lens, spaced by the sum of their focal lengths, to create an inverted afocal system with an angular magnification of the ratio of the primary and secondary lenses. A Galilean telescope uses a negative secondary lens, again spaced by the sum of the primary and secondary lens focal lengths, to create a non-inverting afocal telescope with an angular magnification of the ratio of the primary and secondary lens powers. In both cases, a lower angular resolution camera (lens + focal plane) can be used to record the magnified image.

To create a simple first-order model for the two MMS arrangements, we can consider a one-dimensional (1D) array of thin lens elements and starting parameters: total system FOV, FOV_T, IFOV, wavelength of light, λ, 1D number of pixels per focal plane, N_P, and pixel pitch, p.

Considering a 1D array of secondary optics (eyepiece + array camera), the total number of pixels in 1D is $N_T = \mathrm{FOV}_T/\mathrm{IFOV}$. With the sensor chosen, the number of 1D array elements is then given by $N_A = N_T/N_p$, and the half angle required by each is $\alpha = \mathrm{FOV}_T/2N_A$, where α is the half-FOV per subimager not including any image overlap. The focal length of the array camera will be given by

$$f_{\mathrm{AC}} = \frac{X_S}{2|M|\tan(\alpha)}, \tag{1}$$

where M is the angular magnification of the telescope, $M = -f_o/f_e$, given by the ratio of the focal lengths of the objective and eyepiece and X_S is the 1D focal plane size: $X_S = pN_p$. From Eq. (1), we can see that the total focal length of the MMS lens system is $f_{\mathrm{MMS}} = |M|f_{\mathrm{AC}} = |f_o/f_e|f_{\mathrm{AC}}$. To resolve the pixel pitch of the focal plane, we can use the Rayleigh criterion to specify a maximum $F/\#$ for the array camera, which is also the $F/\#$ for the overall system, $F/\#_{\mathrm{AC}} = p/1.22\lambda$. Combining this condition with Eq. (1) gives the required aperture of the array camera,

$$D_{\mathrm{AC}} = \frac{0.61 \cdot N_p\lambda}{|M|\tan(\alpha)}. \tag{2}$$

The packing of the array and the FOV of the array camera determine the aperture of the eyepiece. The maximum eyepiece aperture, mechanically and for most effective light collection, occurs when the eyepiece is in contact with the adjacent eyepiece lenses of the array

$$D_{\mathrm{EP}} = 2d\ \tan(\alpha), \tag{3}$$

where D_{EP} is the diameter of the eyepiece, and d is the separation between the objective and eyepiece as shown in Fig. 1. To determine the remaining model parameters we must consider vignetting within the system and tradeoffs in the particular system geometry.

A. Keplerian-Type Model

In the traditional Keplerian arrangement the stop and entrance pupil are located at the objective, placing the exit pupil at the eye (array camera in our case) with eye relief, $l_{\mathrm{relief}} = -d/M$ [17]. Vignetting and the FOV of the telescope with the stop in the objective are determined by the size of the telescope eyepiece. With a MMS lens system the eyepiece is limited in size and packing of the adjacent eyepiece lenses of the array, and the frequency of the array is determined by the FOV covered by each array camera. With the stop in the objective and adjacent array eyepieces in contact, 50% vignetting occurs at the transition between array cameras. Dashed lines in Fig. 1 show the path of the chief ray to the eyepiece at the FOV of the array camera. The onset of vignetting occurs at a field angle of

$$\alpha_{\mathrm{Vonset}} = \frac{D_{\mathrm{EP}} - D_{\mathrm{AC}}}{2d}. \tag{4}$$

In addition to the vignetting associated with transitioning between array cameras, a MMS lens with the stop in the objective will incur a $\cos(\theta)$ falloff in relative illumination (RI) due to the obliquity of the aperture stop. Figure 2 shows an example first-order

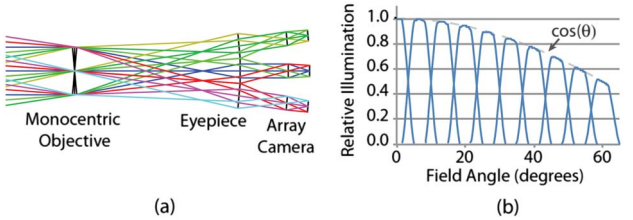

Fig. 2. (Color online) Keplerian-type with stop in objective. (a) Layout showing three subimagers, and (b) relative illumination for a full field of ±60°.

Keplerian design with its associated RI showing the large variations in RI between subimagers and across the full FOV.

Vignetting is traditionally reduced in Keplerian telescopes with the use of a field lens placed close to the intermediate image. Field lenses can be added to the Keplerian-type MMS design to completely eliminate the vignetting between subimagers provided that there are no gaps, i.e., sharp transitions, between adjacent field lenses. With a field lens the eye relief to place the exit pupil at the array camera is

$$l_{\text{relief,FL}} = \frac{-d}{M} - \frac{f_{\text{EP}}^2}{f_{\text{FL}}}, \tag{5}$$

where f_{FL} is the focal length of the field lens given by

$$f_{\text{FL,max}} = \frac{f_{\text{EP}}^2}{\frac{-d}{M} + \frac{D_{\text{EP}} - D_{\text{AC}}}{2M \tan \alpha}}. \tag{6}$$

The value of f_{FL} in Eq. (6) is a maximum, representing the lowest power and least aberrating field lens to achieve zero vignetting in the MMS camera.

Although field lenses can correct problematic variations in RI across the full stitched image, a single-piece, precision hemispherical array of field lenses with the necessary sharp transitions and tight tolerances is a difficult and high-risk task with current fabrication capabilities [18]. An attractive alternative approach to improve vignetting and RI without field lenses is to place the stop at each array camera instead of the monocentric lens. In terms of the overall multiscale design this can be thought of as local control rather than global control of the light bundle. With a local stop at the array camera, the objective lens now appears identical to each subimager and there is no $\cos(\theta)$ obliquity factor across the full FOV. In addition, vignetting between adjacent subimagers can be reduced to zero as light is allowed to fill the local stop at the array camera. A consequence of this reduction in vignetting is a departure from the monocentric condition for the objective within each local imaging path. In this way the monocentric condition applies globally rather than locally for each subimager. A first-order Keplerian-type design example with the stop at the array camera is shown in Fig. 3. Since there is no geometrical vignetting the roll-off in RI at the transitions between subimagers is well approximated by the cosine fourth law of the array camera alone [Fig. 3(b)].

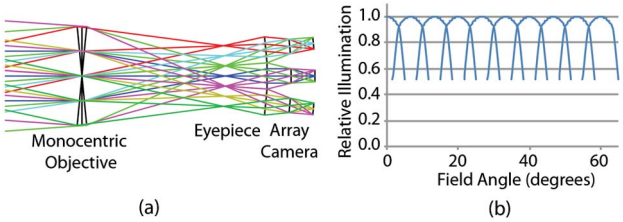

Fig. 3. (Color online) Keplerian-type with stop at the array camera. (a) Layout showing three subimagers, and (b) relative illumination for a full field of ±60°.

For zero vignetting with the stop at the array camera, the array camera and eyepiece must be arranged as shown in Fig. 4(a) with the relationship

$$\tan(\alpha') = \frac{D_{\text{EP}} - D_{\text{AC}}}{2l_{\text{relief}}}, \tag{7}$$

where α' is the magnified field angle at the array camera given by

$$\alpha' = \tan^{-1}(|M| \tan(\alpha)). \tag{8}$$

Combining with expressions for the eyepiece and array camera diameters gives the eye relief for zero vignetting:

$$l_{\text{relief}} = \frac{f_o}{M^2} - \frac{f_o}{M} - \frac{X_S}{4M^2 \text{F/\#}_{\text{AC}} \tan^2(\alpha)}. \tag{9}$$

With the stop and exit pupil at this location with exit pupil diameter, $D_{\varepsilon'} = D_{\text{AC}}$ the entrance pupil will be moved to the location

$$l_\varepsilon = \frac{MD_{\text{AC}}}{2 \tan(\alpha)}, \tag{10}$$

in front of the objective with a diameter given by $D_\varepsilon = |M| D_{\text{AC}}$. The diameter of the objective lens required for zero vignetting is found from the location and size of the entrance pupil to be

$$D_o = \frac{X_S}{F/\#_{\text{AC}} \tan(\alpha)} = 2D_\varepsilon, \tag{11}$$

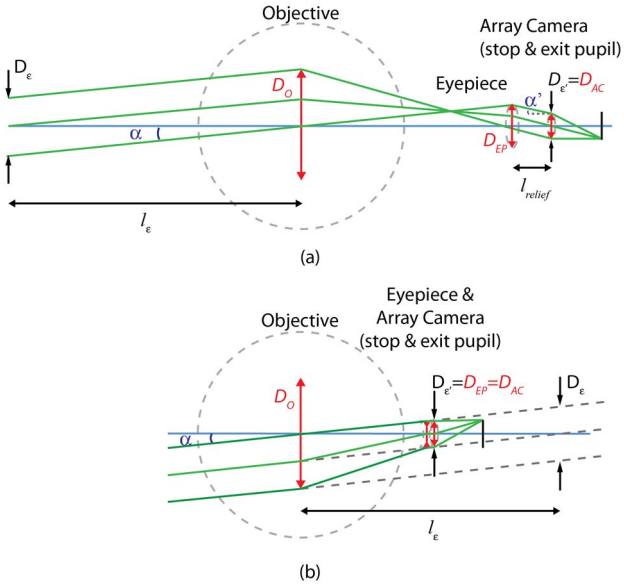

Fig. 4. (Color online) Detail for calculation of vignetting with stop at the array camera. (a) Keplerian-type at the onset of vignetting, and (b) Galilean-type at the onset of vignetting.

which is twice as large as the entrance pupil diameter, D_ε.

B. Galilean-Type Model

In a traditional Galilean telescope the eye is the stop and exit pupil of the system. In our case the stop and exit pupil are placed at the array camera (analogous to the eye). With the stop located at the array camera, vignetting is determined by the size of objective lens's aperture. With a Galilean-type MMS system we can first assume that no eye relief is necessary ($l_{\text{relief}} = 0$) since additional eye relief only increases vignetting for a given objective lens diameter. Since the eyepiece and array camera are collocated, and ultimately combined, we can also assume that they have the same diameter, $D_{\text{EP}} = D_{\text{AC}}$, which specifies a magnification for ideal packing:

$$M_{\text{opt}} = \frac{X_s}{4f_o \tan^2(\alpha) F/\#_{\text{AC}}} \frac{1}{} + 1. \tag{12}$$

This value of magnification is an optimum since larger values cannot be achieved without reducing D_{AC} and smaller values increase wasted space and vignetting for a given objective aperture size. In addition, there is a physically constrained minimum for the magnification since the eyepiece must be located outside the monocentric objective. For example, magnification will be constrained to approximately $M_{\text{opt}} \geq 2$ for dual material monocentric designs, and $M_{\text{opt}} \geq 3$ for single material monocentric designs based on the diameter of the objective lens. With the Galilean-type design, the entrance pupil will be located at, $l_\varepsilon = Md$, behind the objective lens with aperture $D_\varepsilon = MD_{\text{AC}}$ as shown in Fig. 4(b). The field angle where vignetting just begins is given by

$$\tan(\alpha) = \frac{(D_o/2) - M(D_{\text{EP}}/2)}{Md}. \tag{13}$$

Rearranging Eq. (13), the diameter of objective lens, D_o, for zero vignetting is equivalent to Eq. (11), the value for the Keplerian-type design with the stop at the array camera.

C. Considerations for Two-Dimensional Tiling

The preceding discussion dealt with a 1D tiling for simplicity. Real designs with two-dimensional (2D) tiling are significantly more complex and require an adequate solution to the Tammes problem to maximize the sphere packing density [19]. One practical scheme uses a modified icosahedral geodesic to achieve high packing density with a combination of hexagonal and pentagonal tiling, and irregular spacing over the hemispherical array of subimagers [20,21]. The design parameters given by the 1D tiling equations understate the vignetting and RI of a real system due to the larger subimager separations in certain directions, such as those along hexagonal vertices, and irregular packing. Figure 5 illustrates by example possible variations in RI due to field

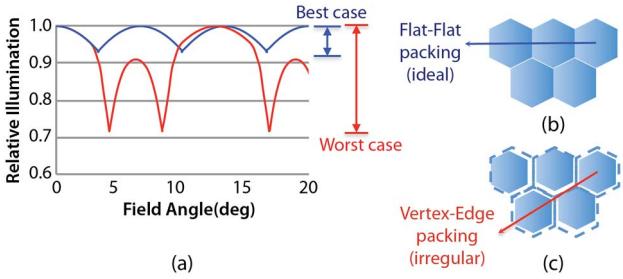

Fig. 5. (Color online) (a) Relative illumination for (b) flat-flat field orientation with ideal hexagonal packing, and (c) vertex-edge field orientation with a 15% spacing irregularity.

direction and irregularity. Such variations in RI for 2D tiling are significant, but can be estimated based on the packing scheme and are generally reasonable when the zero vignetting 1D equations are used as a design starting point. When using the modified icosahedral geodesic packing scheme, the most area-efficient shape for tiling sensors to cover the 2D image field is a hexagon, as shown in Fig. 5. While it is possible to make hexagonal focal planes, approximately 35% of the pixels in a conventional 4:3 aspect ratio sensor would either be redundant and used for image stitching or not illuminated.

3. System Scaling

A. Monocentric Multiscale Lens Systems

Once the starting parameters have been chosen, the optical designer must choose values for the free parameters of the system to fully define the first-order model. For the Keplerian-type there are two free parameters: magnification (M) and the $F/\#$ of the objective lens given by

$$F/\#_o = \frac{f_o}{D_\varepsilon} = \frac{2f_o}{D_o}, \tag{14}$$

assuming the object at infinity. The Galilean-type has only one free parameter, $F/\#_o$ Eq. (14), since magnification is fixed to an optimal value given by Eq. (12). $F/\#_o$ is practically limited in a MMS lens by the structure and performance of the monocentric lens. It is sometimes suggested that the $F/\#$ of an imaging lens tends to be approximately the cube root of its focal length, $F/\#_o = \sqrt[3]{f_o}$ [5,22]. While not a constraint and often inaccurate, this rule of thumb can be useful for choosing a design starting point. If combined with Eq. (11) and Eq. (14), $F/\#_o$ is eliminated as a free parameter. In this discussion of scaling we will leave $F/\#_o$ as a free parameter to examine its effect. In addition, since the aperture of the objective, D_o, is required to be 2× the entrance pupil diameter for zero vignetting, values of $F/\#_o < 3$ are not realistic with a crown/flint monocentric triplet (see Sec 4 for an example). Smaller values of $F/\#_o$ are possible with single element ball lenses; however we will constrain our discussion to achromatized monocentric

triplets which are better suited to gigapixel scale resolutions.

Although magnification is a free parameter in the Keplerian-type design, it has a geometrically constrained minimum value when the eye-relief Eq. (9) goes to zero:

$$|M_{\min}| = \frac{1}{2F/\#_o \tan(\alpha)} - 1. \tag{15}$$

The minimum values of magnification are plotted in Fig. 6(a) as a function of 2D resolution where we have chosen a specific sensor geometry ($N_p = 2800$ pixels, with pitch $p = 1.4$ μm) typical of current commercially available CMOS image sensors. 2D resolution is estimated as $N_{T,2D} = \frac{\pi}{4} N_T^2$, assuming symmetric FOV. In addition to this geometrical constraint on the minimum value of magnification, values of magnification less than or equal to one ($M \leq 1$) have no practical significance since the system could be replaced with a smaller and simpler multicamera array. The potential advantage to the MMS arrangement is linked to the value of this magnification and practically requires larger values.

As previously noted, magnification for the Galilean-type is constrained to be $M_{\text{opt}} \geq 2$ by the physical separation of the monocentric objective and the eyepiece lens. Figure 6(b) shows the optimal magnification of the Galilean-type, given by Eq. (12), as a function of 2D resolution. Note that the optimal magnification of the Galilean-type and the minimum magnification of the Keplerian-type are simply related: $M_{\text{opt}} = |M_{\min}| + 2$.

The optical volume of Keplerian and Galilean-type MMS lenses can be calculated as the volume sum of a front hemisphere with the radius of the objective and a larger partial rear hemisphere with a radius totaling the track length of the rear concentric optics (objective, eyepiece and array camera). The partial rear hemisphere is made up of a cylinder and a spherical cap (Fig. 6 includes a sketch) [23]. Assuming 120° FOV_T, some geometric manipulation gives the total optical volume of the system as

$$\text{Volume} = 2.09 r_f^3 + 1.8325 r_b^3, \tag{16}$$

where r_f is the front radius of the monocentric lens and r_b is the distance from the center of the monocentric lens to the final image plane. Assuming a specific but common monocentric triplet, such as the one described in Sec. 4, we find that the front radius and focal length are related as $r_f \approx 0.475 f_o$ For the Keplerian-type design, r_b will be given by the sum of parameters d, l_{relief} and f_{AC}, or

$$r_{b,\text{Keplerian}} = \frac{X_S}{2\tan(\alpha)}\left[\frac{F/\#_o}{F/\#_{\text{AC}}}\left(1 - \frac{1}{M}\right)^2 - \frac{1}{M} - \frac{1}{2M^2 F/\#_{\text{AC}} \tan(\alpha)}\right]. \tag{17}$$

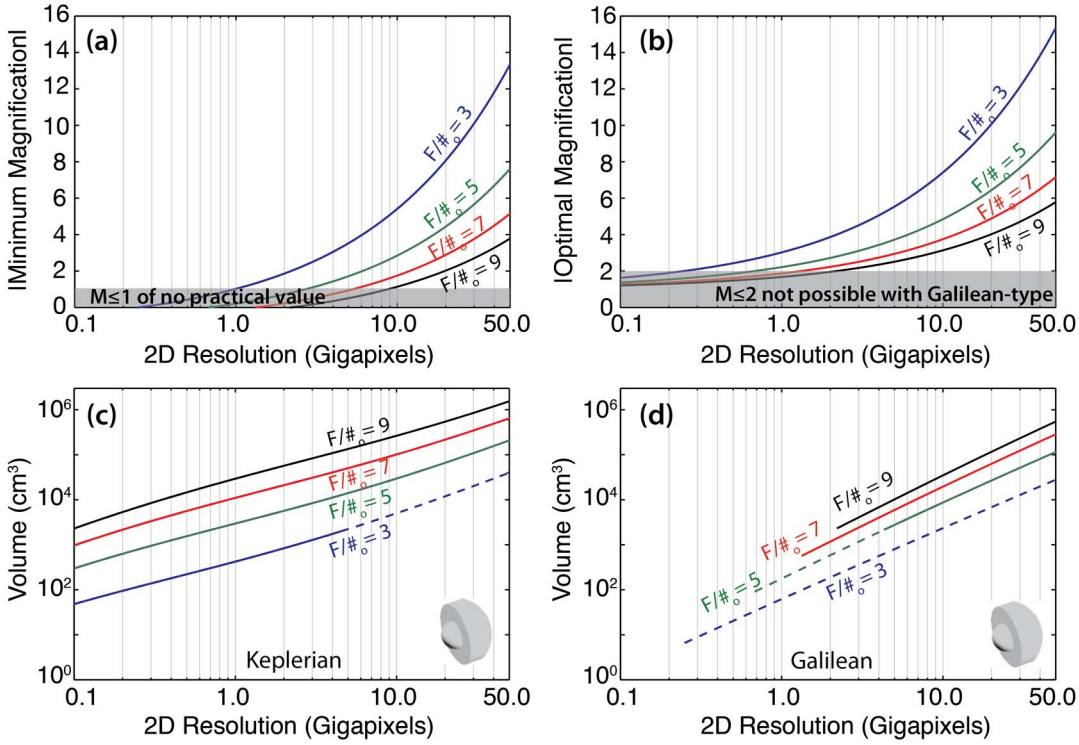

Fig. 6. (Color online) Scaling of first-order model parameters for fixed sensor size ($N_p = 2800$, $p = 1.4$ μm). (a) Keplerian-type minimum required magnification versus 2D resolution, (b) Galilean-type optimal magnification vs. 2D resolution, (c) Keplerian-type optical volume vs. 2D resolution and (d) Galilean-type optical volume vs. 2D resolution. (c) and (d) both use the "optimal" value of magnification from (b) for comparison. Solid line volume curves (c and d) represent more realistic sensor packing requirements due to sensor packaging ($\rho = 2$). Dashed line volume curve represents the extension to the curve possible when the sensor package is not included ($\rho = 1$).

For the Galilean-type design r_b will be given by the sum of parameters d, and f_{AC} or

$$r_{b,\mathrm{Galilean}} = \frac{X_S}{2\tan(\alpha)}\frac{F/\#_o}{F/\#_{\mathrm{AC}}}\left[1-\frac{1}{M}+\frac{F/\#_{\mathrm{AC}}}{F/\#_o M}\right]. \quad (18)$$

Further, sensor packing presents a practical constraint particularly when the packaging of the image sensors is taken into account. This constraint can be expressed by enforcing a value of r_b large enough to allow for separation between the image sensors:

$$r_b \geq \frac{\rho X_S}{2\tan(\alpha)}, \quad (19)$$

where ρ is a scaling factor representing the size of the image sensor package compared to the active pixel array.

Figures 6(c) and 6(d) show volume scaling as function of 2D resolution for the Keplerian-type and Galilean-type designs, respectively, using the same fixed sensor size ($N_p = 2800$, $p = 1.4$ μm). To make the charts as comparable as possible, the "optimal" magnification of the Galilean-type Eq. (12) was used for both. Comparing the charts shows well defined boundaries for the Galilean-type on the lower end of its scaling for fixed sensor size due to the magnification constraint ($M_{\mathrm{opt}} \geq 2$). The curves also show the effect of the sensor packing constraint (Eq. (19)) with the dashed line representing an ideal sensor without additional packaging ($\rho = 1$) and the solid line representing the more realistic situation with a sensor package twice as large as the active pixel array ($\rho = 2$). As expected this constraint is more severe for the Galilean-type arrangement since it is more closely packed than the Keplerian arrangement. This constraint occurs for the Galilean-type at lower aggregate resolutions, while at larger resolutions for the Keplerian-type. This is due to the fact that increased magnification, which is generally necessary for a larger aggregate resolution, expands the Galilean-type and compacts the Keplerian-type architecture. This analysis suggests that although the Galilean-type architecture is attractive due to its smaller overall size, it is much more constrained than the Keplerian-type arrangement and more likely to be impractical when items such as the optomechanics, electronics, focus mechanisms and so on are considered.

Figure 7 shows volume as a function of objective $F/\#$ and magnification for 2 gigapixel (a) and 50 gigapixel (b) Keplerian-type designs, again with the same fixed sensor ($N_p = 2800$, $p = 1.4$ μm, $\rho = 2$). These plots indicate the system scaling possible by varying optical power and the apparent broader design space at 2 gigapixels resolution, due to the minimum magnification (Eq. (15)) and sensor packing (Eq. (19)) constraints.

B. Comparison to a Multicamera Array

The importance of the MMS architecture for wide-angle high-resolution imagers is best demonstrated compared to a multicamera array, where cameras with independent optics each sample a portion of the FOV. Using the same starting parameters described in Sec. 2, each camera of the multicamera array will have a focal length described by

$$f_{\mathrm{MCA}} = \frac{X_S}{2\tan(\alpha)} \quad (20)$$

and an aperture diameter given by

$$D_{\mathrm{MCA}} = \frac{0.61 \cdot N_p \lambda}{\tan(\alpha)}. \quad (21)$$

Assuming that the cameras are distributed on a curved surface, the area and volume of the multicamera array depend primarily on the spacing of the camera elements. For lower overall resolution systems with larger angular field per sensor, α, the sensor package will limit the spacing. As the overall system resolution increases with fixed identical array sensors, there will be a point, $F/\#_{\mathrm{MCA}} = 1/2\rho\tan(\alpha)$, where the diameter of the optics becomes larger than the sensor package and dominates the camera spacing. The scaling factor ρ is once again included to represent the size of the package compared to the pixel array; with typical

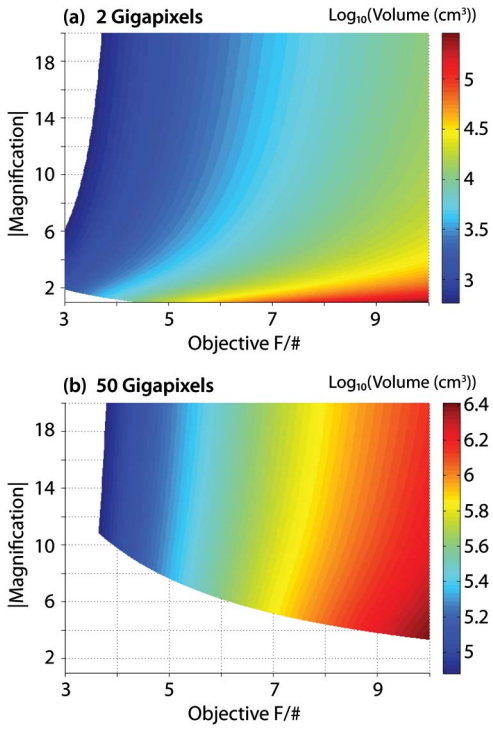

Fig. 7. (Color online) Effect of objective $F/\#$ and telescope magnification on optical volume for Keplerian-type designs at (a) 2 gigapixels and (b) 50 gigapixels aggregate resolution. Identical fixed sensor size and packaging used for both ($N_p = 2800$, $p = 1.4$ μm, $\rho = 2$).

values of about 2 for the smaller array height in CMOS image sensors. The 2D area that the multicamera array occupies is then estimated to be

$$\text{Area}_{\text{MCA,optics lim}} = \frac{\left(\frac{3}{2}N_A D_{\text{MCA}}\,\sin(\text{FOV}_T/2)\right)^2}{\pi} \tag{22}$$

when the camera spacing is dominated by the optics aperture, and

$$\text{Area}_{\text{MCA,sensor lim}} = \frac{\left(\frac{3}{2}N_A(\rho X_S)\,\sin(\text{FOV}_T/2)\right)^2}{\pi} \tag{23}$$

when the camera spacing is limited by the sensor package. The optics volume of the multicamera array is estimated to be

$$\text{Volume}_{\text{MCA,optics lim}} = \pi f_{\text{MCA}}\left(\frac{N_A D_{\text{MCA}}}{2}\right)^2 \tag{24}$$

when the camera spacing is dominated the by the optics aperture, and

$$\text{Volume}_{\text{MCA,sensor lim}} = \pi f_{\text{MCA}}\left(\frac{N_A(\rho X_S)}{2}\right)^2 \tag{25}$$

when the camera spacing is dominated by the sensor package. Figure 8 shows a comparison between the multicamera and Keplerian MMS imager architectures using 8 megapixel square focal planes with 2800 pixels in 1D and a pixel pitch of 1.4 um. Because of the Rayleigh criterion based on the pixel pitch, both architectures are $F/2.1$ at the image plane. This comparison assumes that both the multicamera array and MMS imager had optimal sensor area formats. If both systems use a conventional 4:3 aspect ratio focal plane, the array camera volume (and area) could be reduced by approximately 35% by matching the horizontal and vertical angle pitches to the focal plane's asymmetric shape.

In Fig. 8 there is crossover point where the area and volume of the MMS lens architecture become advantageous compared to the multicamera array. This point occurs shortly after the transition point for the multicamera array, where the diameter of the optics begin to dominate the size of the array needed to resolve the IFOV on the chosen pixel pitch. At resolutions significantly larger than the crossover, the scaling advantage of the MMS lens architecture becomes dramatic, especially in diameter and area of the array. For example, Fig. 9 shows a size comparison between the multicamera array and MMS system at 50 gigapixels. At 50 gigapixels the multicamera array measures roughly 6.2 m in diameter compared to a diameter of 1.6 m for the MMS system using the "optimal magnification" of Fig. 6(b) and an

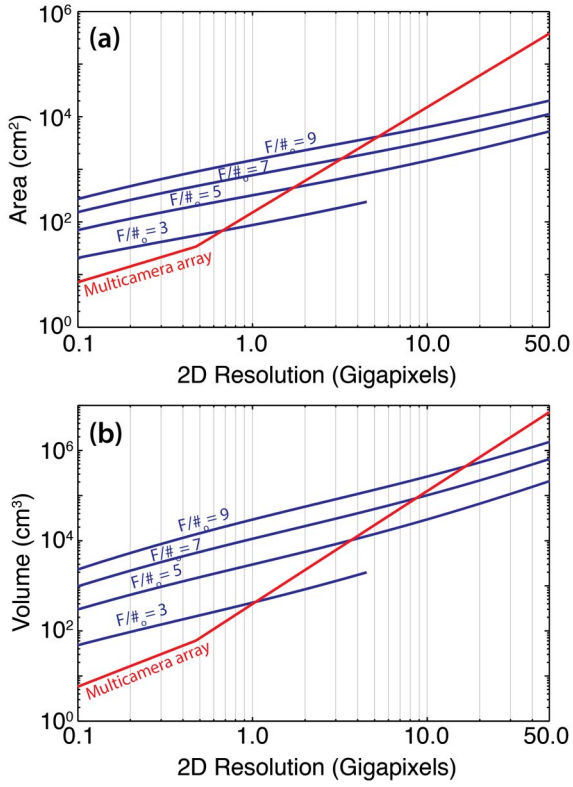

Fig. 8. (Color online) Area and volume as a function of 2D resolution comparing the Keplerian MMS imager architecture (blue curves) and the multicamera array architecture (red curve) for fixed sensor size ($N_p = 2800$, $p = 1.4$ μm, $\rho = 2$). (a) 2D projected optical area, and (b) optical volume. Both system architectures are $F/2.1$ at the image plane.

$F/\#_o$ of 9 (chosen using the $F/\#_o$ rule of thumb from Sec. 3.A). Both example systems are $F/2.1$ at the image plane. The simple explanation for this dramatic difference is that the largest optical element is shared between all array elements in the MMS lens architecture, creating a significant advantage when the required aperture is much larger than the focal plane. At smaller resolutions, such as the 2 gigapixel example in this paper, the comparison is less dramatic, but it is clear that the MMS lens structure has important advantages for very large pixel count wide-field cameras.

4. Design Example: MOSAIC 2 Gigapixel Camera

In this section we present the detailed design of a MMS imager currently being constructed for DARPA's AWARE program. The MMS design resolves more than 2 gigapixels at an IFOV of 41.5 μrad over a symmetric FOV of 120°, using 226 14 megapixel CMOS image sensors. In Sec. 3.A we showed that the MMS lens architecture has significantly better scaling behavior compared to a multicamera array for wide FOV, small IFOV systems due to its shared largest aperture. At 2 gigapixels, this advantage is less clear with a first-order MMS having a smaller area but larger volume than a first-order multicamera array (Fig. 8). This design serves as a practical

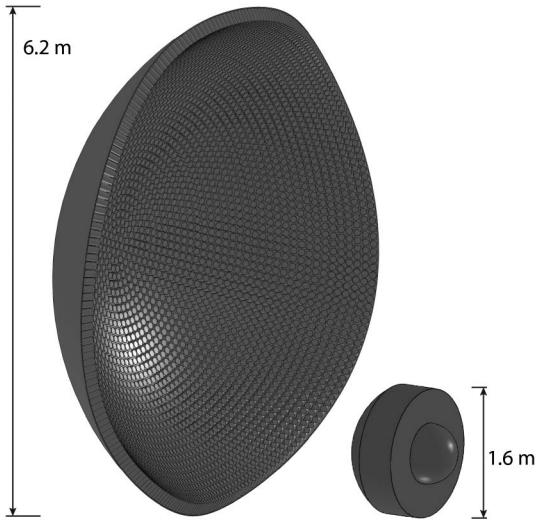

Fig. 9. Size comparison at 50 gigapixels aggregate resolution over 120° symmetric field of view. (Left) 50 gigapixel multicamera array: 6,360 independent 8 megapixel cameras each 84 × 168 mm. 6.2 m diameter for full 120° concave array. (Right) 50 Gigapixel monocentric multiscale imager: 6,360 common aperture 8 megapixel imagers. 1.6 m system diameter at $M = 5.8$, $F/\#_o = 9$. Both system architectures are $F/2.1$ at the image plane.

first demonstration of the concept and a step toward even larger pixel count wide-FOV systems. We will constrain this section to a discussion of the specifics of the optical design. A preliminary discussion of the digital image reconstruction and array stitching for this camera can be found elsewhere [24].

A. Design and Optical Performance

The monocentric triplet objective of this design consists of a fused silica (crown) ball lens core and an Ohara SNBH8 (flint) external shell optimized for minimal spherical and axial chromatic aberration using ZEMAX [25]. The radii of curvature of the front and back SNBH8 shells differ slightly—31.8 mm and 33.378 mm respectively—giving a small front-to-back asymmetry, which provides an improved solution for the object at infinity. The objective lens has an effective focal length of 70.25 mm, and focuses to a

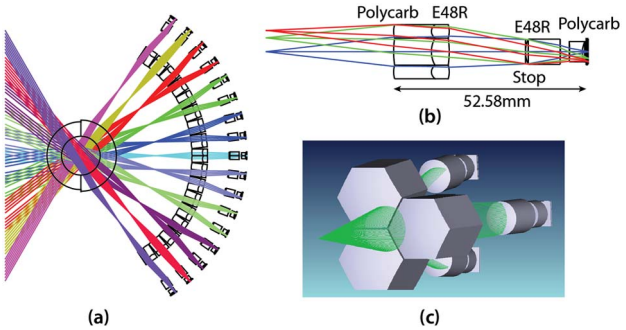

Fig. 10. (Color online) Layout of the MOSAIC 2 gigapixel MMS lens design. (a) Multiscale arrangement showing monocentric objective and surrounding subimagers; (b) 4-element injection-molded subimager layout, and (c) perspective view showing hexagonal tiling and light sharing of subimagers.

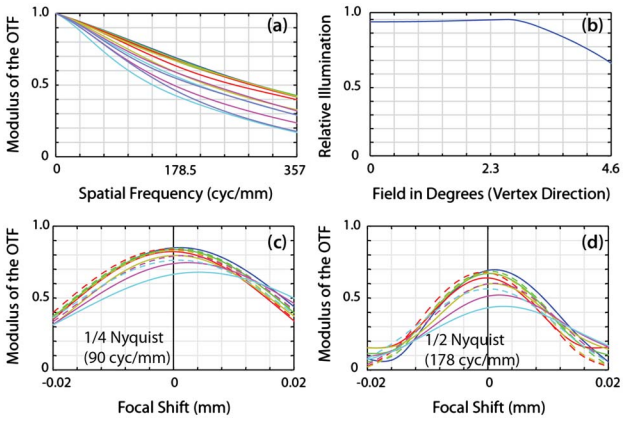

Fig. 11. (Color online) Single channel performance for the MOSAIC 2 gigapixel MMS lens system. (a) Polychromatic MTF (0.47, 0.55, 0.65 μm); (b) Relative illumination over field required in vertex direction; (c) Through-focus polychromatic MTF at 90 cyc/mm (¼ Nyquist), and (d) through-focus MTF at 178 cyc/mm (½ Nyquist). (a), (c) and (d) show Tangential and Sagittal data for field angles of 0° (blue), 1° (green), 2° (red), 3° (light green), 4° (purple) and 4.6° (cyan).

spherical intermediate image plane 70.25 mm from the center of the objective as shown in Fig. 10(a).

The aspheric subimagers that form the array of the MMS lens are shown in Fig. 10(b). Each subimager in the array is made from the same plastic lens parts replicated by injection molding. The first element of the subimager, which functions as the eyepiece, is a plastic cemented doublet of polycarbonate and Zeonex E48R [26] with a hexagonal aperture for close packing at the front plane as shown in Fig. 10(c). With the exception of the center pentagonal element, which must be custom shaped, all of the elements in the array have hexagonal packing. The hexagonal shape of the front element improves the RI for field angles that fall at the vertex of a hexagonal packing scheme, where three subimagers share the circular cone of light from the objective.

The array camera is made of an air-spaced pair of Zeonex E48R and polycarbonate lenses to provide the final image. The front side of the Zeonex lens contains a weak diffractive optical element (DOE) to aid with the chromatic correction of the subimager. The optimized DOE has 36 periods with a minimum diffractive groove pitch of 70 μm suitable for diamond turning and injection molding. The polycarbonate lens of the array camera is a thick meniscus element, functioning both to flatten the field and control the chief ray angle (CRA) to best match the microlenses of the Aptina MT9F001 1/2.3 inch CMOS image sensor used with this design [27]. This image sensor has 4608 × 3688 1.4 μm pixels, with gradually shifted microlenses up to 25° CRA at the sensor's maximum image height.

The stop for this design is 6.4 mm in diameter, located at the front of the array camera to provide acceptable RI (>68%) across the full stitched image as described in Sec. 3. Figure 11 shows performance results: incoherent polychromatic modulation transfer

function (MTF), RI, and through-focus MTF for a single channel of the MMS lens out to a field angle of 4.6° (9.2° FOV) in the vertex direction of the hexagonal packing. This value of 4.6° was determined to be the FOV required per subimager to provide substantial overlap between adjacent subimagers in the array based on the geodesic packing frequency, i.e., the number of subimagers contained in the 120° full system FOV. The minimum center-to-center angular separation between subimagers with this geodesic packing scheme was 7.04°. The magnification of the system was designed such that the required image formed by each subimager fell just inside an inscribed hexagon within the active area of each image sensor. The transverse magnification between the intermediate image plane of the objective and the final image plane is −0.484 (demagnified). The working $F/\#$ for this design is 2.19 on-axis, increasing to 2.61 at the 4.6° edge of the subimager's field due to allowed vignetting. Distortion at the edge of the field is −3.3% (barrel) to be corrected in final post-processing.

B. Tolerances and Refocus

The monocentric objective is made using standard spherical lens polishing technology and can be formed with either three elements, where the central fused silica ball lens is formed monolithically, or four parts, where two hemispherical halves of the ball lens are bonded together. The second of these two options allows for the possibility of an internal stop to be included in the fabrication of the objective. The tolerances for the monocentric objective are ±25 μm decenter or departure from the monocentric condition, and ¼λ irregularity.

The injection-molded lenses of the subimager are mounted into lens barrels to fix the relative positions of the parts. The design of the subimager was optimized for as-built performance with the following tolerances suitable for injection molding: ±12.5 μm surface/element decenters, ±12.5 μm glass/air axial thickness, ±0.05° surface/element tilt, and ±0.001 material index of refraction [28]. Using these tolerances, a root-sum-square sensitivity method estimates a root-mean-squared (RMS) wavefront change from the nominal 0.095 to 0.139. Monte Carlo analysis of the system suggests reasonable insensitivity to the above tolerances maintaining on-axis MTF > 0.65, 70% field MTF > 0.38, and 90% field MTF > 0.15 at half Nyquist (178 cyc/mm). At full Nyquist, on-axis MTF > 0.28, 70% field MTF > 0.15, and 90% field MTF > 0.05 at 357 cyc/mm.

The positioning tolerance of each subimager's barrel in relation to the monocentric objective was found to be ±300 μm decenter (or monocentric axis deviation), ±150 μm axial, and ±0.12° tilt. Although these values are large, they represent local tolerances for subimager performance and do not ensure complete image overlap for processing of the final image. System (global) alignment tolerances are more complex since they depend on the geodesic packing, sensor size, and orientations and the tolerance stack up within each subimager. These issues will be discussed further in a subsequent paper describing construction of the MOSAIC camera system.

Simple refocus is accomplished by axial positioning of the CMOS image sensor at the back of each subimager's lens barrel. This design is capable of refocus over a range from infinity to 15 m with a +70 μm change in the axial position of the sensor. This range can be improved to better than 5 m if the focus adjustment is moved to adjust the spacing between the last two elements of the subimager as opposed to the sensor position.

C. Comparison to First-Order Model

Table 1 shows a parameter comparison between a 2 gigapixel afocal first-order model, and a modified first-order model describing the MOSAIC design of this section. In this case, the MOSAIC design preceded the first order model and was not constrained to be afocal at the stop. Instead it is *almost* afocal, making a somewhat loose but useful comparison possible. To compare as closely as possible, the first seven parameters of Table 1 were matched as design starting parameters using the flat-to-flat subimager orientation of the final design. The parameters in the left-hand column were calculated from the afocal parameters of Secs 2 and 3 while the first-order parameters for the MOSAIC design in the middle column were calculated from the lens elements of the final design. The first-order afocal model shows good agreement with the final design with notable differences occurring in the objective-eyepiece distance (d), and the focal length (f_{AC}) of the array camera, which display the deviation from the afocal condition. These changes account well for the increased optical volume and vignetting [see Fig. 11(b)] of the MOSAIC design compared to the first-order model.

Table 1. Comparison Between First-Order Model Parameters for the 2 Gigapixel MOSAIC Design

	First-Order Afocal Model	Modified First Order Model (not afocal)	MOSAIC Design (actual)
FOV_T	120°	120°	
IFOV	41.5 μrad	41.5 μrad	
α	3.4°	3.4°	
p	1.4 μm	1.4 μm	
X_S	4.0 mm	4.0 mm	
$F/\#_o$	4.4	4.4	
M	2.5	2.5	
$F/\#_{\mathrm{AC}}$	2.1	2.1	
D_o	33.2 mm	33.9 mm	
f_o	73.4 mm	70.3 mm	
f_{EP}	29.4 mm	27.7 mm	
D_{EP}	12.5 mm	12.5 mm	
d	103 mm	111 mm	
l_{relief}	20.8 mm	19.5 mm	
f_{AC}	13.3 mm	24.6 mm	
D_{AC}	6.1 mm	7.0 mm	
M_r[a]	−0.45	−0.47	
Volume	4702 cm^3	6915 cm^3	7043 cm^3

[a]Magnification between intermediate image and final image.

Comparing the volume of the modified first-order model to the actual volume of MOSAIC final design, shown in the right-hand column of the Table 1, yields an error of less than 2%. The complete optical prescription data for the 2 gigapixel MOSAIC camera is included in Table 2, Table 3, and Table 4 below.

5. Conclusion

In this paper, we have developed a systematic approach to the design of monocentric multiscale imagers including first-order geometrical optical effects, especially vignetting, to specify candidate systems for full optical design. We have identified two classes of MMS imagers, those with and without and internal image plane, and shown how the optical system volume scales with the key parameters of component lens $F/\#$ and telescopic magnification. We have illustrated this design space with a fully toleranced optical design of a diffraction limited MMS lens, which is the basis of a 120° FOV, 41.5 μrad IFOV, 2 gigapixel imager currently under construction. We conclude that with further development of computational image processing, and with the use of advanced fabrication and assembly techniques, MMS lens architectures show promise for wide-angle imagers with aggregate resolutions to well over 50 gigapixels.

This work has been supported by DARPA via the Advanced Wide FOV Architectures for Image Reconstruction (AWARE) program, and is part of a collaborative effort on real-time gigapixel imagers including researchers from Duke, UCSD, RPC Photonics, Inc.,

Table 2. Single Path Prescription Data for 2 Gigapixel MOSAIC Camera (Sec. 4)

Surf. #	Comment	Rad of Curv. (mm)	Thick. (mm)	Material	Diam. (mm)
1	Ball lens	31.8	13.613	S-NBH8	63.6
2		18.187	18.187	F_Silica	36.374
3		Infinity	18.187	F_Silica	36.374
4		−18.187	15.191	S-NBH8	36.374
5		−33.378	36.878	Air	66.756
6	Int. image	Infinity	33.226	Air	—
7	Eyepiece	22.51297	8.386424	Polycarb	14.4[a]
8		8.077042	8	E48R	14.4[a]
9		−25.16423	18.527	Air	14.4[a]
10	IR cut	Infinity	1	Bk7	8
11	Stop	Infinity	0	Air	6.4
12[b]	Array camera	8.097214	9.284709	E48R	7
13		−43.31043	2.482625	Air	6.6
14		−66.75502	3.374655	Polycarb	5.6
15		4.710791	1	Air	5.332
16	Focus	Infinity	0.00816865	Air	5.139
17	Sensor	Infinity	0.4	Bk7	7
18		Infinity	0.125	Air	7
20	Image	Infinity	—	Si	6.6

[a]Vertex-to-vertex distance on hexagonal aperture.
[b]See Table 4 for DOE prescription.

Table 3. Single Path Prescription Data for 2 Gigapixel MOSAIC Camera (Sec. 4): Aspheric Terms

Surf. #	Comment	r^4 Aspheric Term	r^6 Aspheric Term	r^8 Aspheric Term	r^{10} Aspheric Term
7	Eyepiece	$-2.8147152 \times 10^{-5}$	$-4.0237714 \times 10^{-7}$	4.4135689×10^{-9}	—
8		7.2425919×10^{-5}	-1.352871×10^{-5}	1.0086073×10^{-7}	—
9		$-1.6062121 \times 10^{-5}$	1.0507867×10^{-6}	$-1.2540803 \times 10^{-8}$	—
12[a]	Array camera	$-8.1858462 \times 10^{-6}$	4.9291849×10^{-7}	$-6.1449905 \times 10^{-8}$	5.1302673×10^{-9}
13		0.00049936384	$-6.6577601 \times 10^{-6}$	6.2804293×10^{-7}	3.7586356×10^{-8}
14		−0.0026541057	0.00016173157	$-5.9078789 \times 10^{-6}$	4.0337124×10^{-7}
15		−0.0065076023	0.00045055736	$-4.2893373 \times 10^{-5}$	3.5191145×10^{-6}

[a]See Table 4 for DOE prescription.

Table 4. Single Path Prescription Data for 2 Gigapixel MOSAIC Camera (Sec. 4): DOE[a]

Surf.#	Comment	Max Rad. Ap. (mm)	p^2 "Binary 2" Term	p^4 "Binary 2" Term	p^6 "Binary 2" Term
12	Array camera	4.4460065	−250.9302	18.164982	5.2014151

[a]See ZEMAX Optical Design Program User's Manual, Chap. 11, p. 284 (Radiant ZEMAX LLC, July 8 2011).

Distant Focus Corporation, the University of Arizona, MIT, Teledyne, Raytheon, SAIC, and Aptina. This optical design work has been assisted by Michael Gehm, Dathon Golish, and Esteban Vera at UAZ; Jungsang Kim, Hui Son, and Joonku Hahn at Duke; Ron Stack and Adam Johnson at DFC; Bob Gibbons at Raytheon; and Paul McLaughlin and Jeffrey Shaw at RPC Photonics. The authors also acknowledge Kate Baker for assistance with solid modeling. Finally the authors acknowledge helpful discussions on image system architectures and scaling with Joseph Mait and Predrag Milojkovic at the U.S. Army Research Laboratory, and Ravi Athale at MITRE Corporation.

References and Notes

1. R. Sargent, C. Bartley, P. Dille, J. Keller, I. Nourbakhsh, and R. LeGrand, "Timelapse GigaPan: Capturing, sharing, and exploring timelapse gigapixel imagery," presented at *the Fine International Conference on Gigapixel Imaging for Science*, Pittsburgh, PA (2010).
2. V. Suntharalingam, R. Berger, S. Clark, J. Knecht, A. Messier, K. Newcomb, D. Rathman, R. Slattery, A. Soares, C. Stevenson, K. Warner, D. Young, L. P. Ang, B. Mansoorian, and D. Shaver," A
4-side tileable back-illuminated 3D-integrated Mpixel CMOS image sensor, "in *Proceedings of IEEE International Solid State Circuits Conference Technical Digest* (IEEE, 2009).
3. K. W. Hodapp, N. Kaiser, H. Aussel, W. Burgett, K. C. Chambers, M. Chun, T. Dombeck, A. Douglas, D. Hafner, J. Heasley, J. Hoblitt, C. Hude, S. Isani, R. Jedicke, D. Jewitt, U. Laux, G. A. Luppino, R. Lupton, M. Maberry, E. Magnier, E. Mannery, D. Monet, J. Morgan, P. Onaka, P. Price, A. Ryan, W. Siegmund, I. Szapudi, J. Tonry, R. Wainscoat, and M. Waterson, "Design of the Pan-STARRS telescopes," Astron. Nachr. **325**, 636–642 (2004).
4. B. Leininger, J. Edwards, J. Antoniades, D. Chester, D. Haas, E. Liu, M. Stevens, C. Gershfield, M. Braun, J. D. Targove, S. Wein, P. Brewer, D. G. Madden, and K. H. Shafique, "Autonomous real-time ground ubiquitous surveillance-imaging system (ARGUS-IS)," Proc. SPIE **6981**, 69810H (2008).
5. A. W. Lohmann, "Scaling laws for lens systems," Appl. Opt. **28**, 4996–4998 (1989).
6. B. Wilburn, N. Joshi, V. Vaish, E. Talvala, E. Antunez, A. Barth, A. Adams, M. Horowitz, and M. Levoy, "High performance imaging using large camera arrays," ACM Trans. Graph. **24**, 763–776 (2005).
7. D. J. Brady and N. Hagen, "Multiscale lens design," Opt. Express **17**, 10659–10674 (2009).
8. D. L. Marks and D. J. Brady, "Close-up imaging using microcamera arrays for focal plane synthesis," Opt. Eng. **50**, 033205 (2011).
9. J. E. Ford and E. Tremblay, "Extreme form factor imagers," in *Imaging Systems* (Optical Society of America, 2010), paper IMC2.
10. D. L. Marks, E. J. Tremblay, J. E. Ford, and D. J. Brady, "Microcamera aperture scale in monocentric gigapixel cameras," Appl. Opt. **50**, 5824–5833 (2011).
11. Michael Kidger, *Fundamental Optical Design* (SPIE, 2002), Chap. 7.
12. T. Sutton, "On the panoramic lens," a paper read to British Association Report in 1861, as described in Patents for Inventions, Abridgements of the Specifications Relating to Photography (Great Britain Patent Office, 1861).
13. D. L. Marks and D. J. Brady, "Gigagon: A monocentric lens design imaging 40 gigapixels," in *Imaging Systems* (Optical Society of America, 2010), paper ITuC2.
14. G. Krishnan and S. K. Nayar, "Towards a true spherical camera," Proc. SPIE **7240**, 724002 (2009).
15. O. Cossairt, D. Miau, and S. K. Nayar, "Gigapixel computational imaging," in *IEEE International Conference on Computational Photography* (IEEE, 2011).
16. H. Son, D. L. Marks, E. J. Tremblay, J. Ford, J. Hahn, R. Stack, A. Johnson, P. McLaughlin, J. Shaw, J. Kim, and D. J. Brady, "A multiscale, wide field, gigapixel camera," in *Imaging Systems Applications* (Optical Society of America, 2011), paper JTuE2.
17. George Smith and David A. Atchison, *The Eye and Visual Optical Instruments* (Cambridge University, 1997), Chap. 17.
18. W. C. Sweatt, D. D. Gill, D. P. Adams, M. J. Vasile, and A. A. Claudet, "Diamond milling of micro-optics," IEEE Aerosp. Electron. Syst. Mag. **23**, 13–17 (2008).
19. B. W. Clare and D. L. Kepert, "The closest packing of equal circles on a sphere," Proc. R. Soc. A **405**, 329–344 (1986).
20. H. Kenner, *Geodesic Math and How to Use It*, 2nd ed. (University of California, 2003).
21. H. S. Son, D. L. Marks, J. Hahn, J. Kim, and D. J. Brady, "Design of a spherical focal surface using close packed relay optics," Opt. Express **19**, 16132–16138 (2011).
22. O. S. Cossairt, D. Miau, and S. K. Nayar, "Scaling law for computational imaging using spherical optics," J. Opt. Soc. Am. A **28**, 2540–2553 (2011).
23. http://mathworld.wolfram.com/SphericalCap.html.
24. D. Golish, E. Vera, K. Kelly, Q. Gong, D. J. Brady, and M. E. Gehm, "Image formation in multiscaleoptical systems," in *Computational Optical Sensing and Imaging* (Optical Society of America, 2011), paper JTuE4.
25. ZEMAX, Radiant ZEMAX LLC, 112th Avenue NE, Bellevue, Wash. 98004.
26. L. P. Zeon Chemicals, Louisville, Ky. 40211, http://www.zeonchemicals.com/.
27. Aptina Imaging, San Jose, Calif. 95134, http://www.aptina.com/
28. Michael Pfeffer, "Optomechanics of plastic optical components," in *Handbook of Plastic Optics*, S. Bäumer, ed. (Wiley-VCH, 2005).